The Cryosphere Discuss., 8, 537–580, 2014
www.the-cryosphere-discuss.net/8/537/2014/
doi:10.5194/tcd-8-537-2014

The Cryosphere Discussions
Open Access

Hybrid inventory, gravimetry and altimetry (HIGA) mass balance product for Greenland and the Canadian Arctic

W. Colgan[1,2], W. Abdalati[2], M. Citterio[1], B. Csatho[3], X. Fettweis[4], S. Luthcke[5], G. Moholdt[6], and M. Stober[7]

[1]Marine Geology and Glaciology, Geological Survey of Denmark and Greenland, Copenhagen, Denmark
[2]Cooperative Institute for Research in Environmental Sciences, University of Colorado, Boulder, CO, USA
[3]Department of Geology, State University of New York, Buffalo, NY, USA
[4]Department of Geography, University of Liége, Liége, Belgium
[5]Goddard Space Flight Center, National Aeronautics and Space Administration, Greenbelt, MD, USA
[6]Scripps Institution of Oceanography, University of California, San Diego, CA, USA
[7]Stuttgart University of Applied Sciences, Stuttgart, Germany

Received: 3 January 2014 – Accepted: 8 January 2014 – Published: 23 January 2014

Correspondence to: W. Colgan (wic@geus.dk)

Published by Copernicus Publications on behalf of the European Geosciences Union.

Abstract

We present a novel inversion algorithm that generates a mass balance field that is simultaneously consistent with independent observations of glacier inventory derived from optical imagery, cryosphere-attributed mass changes derived from satellite gravimetry, and ice surface elevation changes derived from airborne and satellite altimetry. We use this algorithm to assess mass balance across Greenland and the Canadian Arctic over the December 2003 to December 2010 period at 26 km resolution. We assess a total mass loss of $316 \pm 37\,\mathrm{Gt\,a^{-1}}$ over Greenland and the Canadian Arctic, with $217 \pm 20\,\mathrm{Gt\,a^{-1}}$ being attributed to the Greenland Ice Sheet proper, and $38 \pm 6\,\mathrm{Gt\,a^{-1}}$ and $50 \pm 8\,\mathrm{Gt\,a^{-1}}$ being attributed to peripheral glaciers in Greenland and the Canadian Arctic, respectively. These absolute values are dependent on the gravimetry-derived spherical harmonic representation we invert. Our attempt to validate local values of algorithm-inferred mass balance reveals a paucity of in situ observations. At four sites, where direct comparison between algorithm-inferred and in situ mass balance is valid, we find an RMSD of $0.18\,\mathrm{m\,WE\,a^{-1}}$. Differencing algorithm-inferred mass balance with previously modelled surface mass balance, in order to solve the ice dynamic portion of mass balance as a residual, allows the transient glacier continuity equation to be spatially partitioned across Greenland.

1 Introduction

Greenland is presently the single largest cryospheric source of sea level rise, contributing $0.73 \pm 0.08\,\mathrm{mm\,a^{-1}}$ of sea level rise during the 2005 to 2010 period (Shepherd et al., 2012). Greenland's contribution to sea level rise is believed to have been approximately equally divided between anomalies in meltwater runoff and iceberg calving during the 2000 to 2008 period (van den Broeke et al., 2009). Pursuing a process-level understanding of this contemporary partitioning of mass loss requires characterizing the spatial pattern of mass balance at a sub-basin or glacier scale. This would allow

modelled surface mass balance to be differenced from total mass balance in order to solve for the ice dynamic component of mass change through iceberg calving. Accurate knowledge of the contemporary partitioning of mass loss between meltwater runoff and iceberg calving can serve as a key diagnostic modelling target, in order to improve confidence in subsequent prognostic model simulations.

Three methods are available for assessing mass balance at ice sheet scale: (i) input-output, (ii) volume change, and (iii) gravity change. The first approach, also known as the mass budget approach, differences ice discharge estimated near the grounding line of outlet glaciers from surface mass balance modelled over the ice sheet (e.g. Rignot et al., 2008). The second approach converts surface elevation changes observed by repeat airborne or satellite altimetry into mass changes using an effective density of change estimated through firn density modelling (e.g. Zwally et al., 2011). The third approach uses repeat satellite gravimetry observations and numerous geophysical forward models to assess absolute cryospheric mass changes (e.g. Velicogna and Wahr, 2005). Each method has unique advantages and disadvantages relative to the other methods (Alley et al., 2007). While satellite altimetry characterizes the spatial variability of mass changes at relatively high resolution, it relies on forward modelling of complex firn processes to produce absolute mass changes. Conversely, the absolute cryospheric mass changes observed by satellite gravimetry and isolated by forward models have relatively poor spatial resolution.

Here, we combine the two strengths of gravimetry and altimetry in order to refine absolute measurements of cryosphere-attributed mass change to relatively high spatial resolution. In this process, we overcome two complementary weaknesses: dependence on modelling complex firn processes as well as the fundamental spatial resolution of satellite gravimetry. The mass balance field we derive through an iterative inversion approach is simultaneously consistent with: (i) high spatial resolution ice-sheet and glacier inventory, (ii) gravimetry-derived cryospheric mass change, and (iii) altimetry-derived surface elevation change, at 26 km spatial resolution. We refer to this as a Hybrid Inventory, Gravimetry and Altimetry (HIGA) data product. We suggest that

this 2004 to 2010 mean annual mass balance field may offer the most spatially accurate direct assessment of the combined mass balance of both Greenland and the Canadian Arctic to date.

2 Method

2.1 Data

Our inversion algorithm requires three distinct pieces of input data: (i) fractional ice coverage derived from optical imagery, (ii) cryosphere-attributed mass changes derived from satellite gravimetry, and (iii) ice surface elevation changes derived from satellite altimetry. We compile each of these datasets over a common region of interest focused on Greenland and the Canadian Arctic (Fig. 1). Our time period of interest follows the gravimetry comparison interval adopted by the ice sheet mass balance inter-comparison exercise (IMBIE): December 2003 to December 2010 (Shepherd et al., 2012). We assess mass balance in ten geographic sectors, eight in Greenland and two in the Canadian Arctic. The eight Greenland sectors are equivalent to the eight major ice sheet drainage systems delineated by Zwally et al. (2012), but have been extended beyond the ice sheet margin to also encompass peripheral glaciers and ice caps. The two Canadian Arctic sectors are equivalent to those employed by Gardner et al. (2011). Shapefiles of these ten sector boundaries are available in the Supplement associated with this paper.

We calculated the fractional ice coverage within our study region by clipping object-oriented glacier inventory polygons with a polygon fishnet matching the inversion grid. We then summed the glacierized area within each grid cell, and scaled to correct for projection-related area distortion. In Greenland, we summed peripheral glacier and ice sheet coverage separately. The Greenland glacier inventory data are derived from aerophotogrammetry with a polygon accuracy of 10 m (Citterio and Ahlstrøm, 2013). This inventory classifies glaciers and ice caps demonstrating “no” or “weak” connectiv-

ity with the ice sheet proper as Greenland peripheral glaciers, while glaciers demonstrating "strong" connectivity with the ice sheet are classified as part of the Greenland Ice Sheet proper (cf. Rastner et al., 2012). The Canadian glacier inventory data are derived from the Randolph Glacier Inventory (RGI) version 2.0 (Arendt et al., 2012). We employ both the North and South Canadian Arctic (RGI regions 3 and 4), which are primarily based on Landsat imagery with polygon accuracy of about 30 m. We also use the RGI to calculate fractional ice coverage over Svalbard and a small portion of Iceland (RGI regions 6 and 7) in the far-field of our inversion domain. We take the glacier polygons in both the Citterio and Ahlstrøm (2013) and Arendt et al. (2012) inventories to be representative of ice coverage during the IMBIE period.

The gravimetry-derived cryospheric mass change product we employ is identical to that described in Colgan et al. (2013). This mascon solution is estimated directly from the formal reduction of Gravity Recovery and Climate Experiment (GRACE) K-band inter-satellite range rate (KBRR) data, processing the level 1B (L1B) data, including attitude and accelerometer data. Forward models for ocean tides and ocean mass variations (GOT4.7/OMCT; Ray, 1999), atmospheric mass variations (ECMWF; Ray and Ponte, 2003), terrestrial water storage (GLDAS/Noah; Ek et al., 2003; Rodell et al., 2004) and glacial isostatic adjustment and little ice age correction (ICE-5G; Peltier, 2004) are employed in the L1B data processing in order to isolate land ice mass variations of interest (and, in the case of forward hydrology modeling, limiting correlated residual signal contribution to the land ice solutions). Within Greenland, the trend in each of these corrections is $< 5\,\mathrm{Gt\,a^{-1}}$, and therefore small relative to the trend in cryospheric mass change ($\sim 2\,\%$). Complete details on these forward models and individual trend magnitudes are presented in Luthcke et al. (2013). Covariance constraints are applied by constraint region (e.g. Greenland Ice Sheet and oceans) in order to limit signal leakage in and out across region boundaries. The mascon solution is iterated until convergence when nearly all signal removed from the KBRR residuals (Luthcke et al., 2013).

Following L1B data reduction, the residual cryosphere-attributed linear mass change trend and 1σ trend error are calculated for each mascon time series and subsequently converted into equivalent spherical harmonics of degree and order 60 via a set of differential potential coefficients ("delta coefficients") applied to the mean GRACE level 2 (L2) field (Chao et al., 1987; Luthcke et al., 2013). In comparison to relatively sharp contrasts in mass change characteristic of mascon boundaries, the relatively smooth spatial gradients of spherical harmonics are better suited for the isotropic inversion filter we employ. The GRACE-derived cryosphere-attributed mass change trend we employ is calculated over the IMBIE GRACE comparison period (December 2003 to December 2010; Shepherd et al., 2012). We acknowledge that mascons ultimately provide a better inversion target than mascon-derived spherical harmonics, but we note that a mascon inversion requires an anisotropic geometric filter, and thus represents a non-trivial extension of the isotropic inversion we present.

The satellite altimetry-derived estimates of ice surface elevation change we employ are primarily based on Ice, Cloud and land Elevation Satellite (ICESat) observations from 2003 to 2009. In Greenland, 2 km spatial resolution surface elevation changes are derived from altimetry data following the approach of Schenk and Csatho (2012), which corrects for intermission biases, ground controls and glacial isostatic adjustment. Schenk and Csatho (2012) also incorporate airborne laser observations when and where available. In the Canadian Arctic, 2 km spatial resolution surface elevation changes are derived from ICESat data following the method of Gardner et al. (2011; 2012), with corrections applied for Gaussian-centroid offset (Borsa et al., 2013). Both the Greenland and Canadian Arctic ICEsat observations have been corrected for detector saturation (Fricker et al., 2005). Unlike in Greenland, however, ICESat data (release 633) in the Canadian Arctic are not supplemented by airborne altimetry observations. Across both Greenland and the Canadian Arctic, we average all 2 km resolution surface elevation changes within a given 26 by 26 km grid cell to determine mean ice surface elevation change. In Greenland, an average of 141 values are used to calculate mean surface elevation change within a given grid cell. In the Canadian Arctic, where ice cov-

erage seldom approaches 100 %, an average of 77 values are used to calculate mean surface elevation change within a given grid cell (Fig. 2).

We take the 1σ standard deviation of all rate of surface elevation change observations within a given grid cell as characteristic of the uncertainty in the mean rate of surface elevation change of that grid cell. We determine rate of surface elevation change, as well as this associated 1σ uncertainty, over the IMBIE ICESat comparison period: September 2003 to October 2009 (campaigns 2a to 2f; Shepherd et al., 2012). The IMBIE ICESat comparison period starts nine months after, and ends thirteen months before, the IMBIE GRACE comparison period (~ 13 % shorter). We therefore assume that the spatial distribution of ice surface elevation changes observed during the ICESat comparison period are generally representative of the GRACE comparison period. As firn correction factors are highly spatially correlated, as well as data intensive and difficult to parameterize, we do not correct surface elevation changes for firn densification (or firn air content; e.g. Li and Zwally, 2011). The inversion algorithm effectively uses altimetry-derived surface elevation changes to distinguish relative trends in cryospheric mass changes between adjacent ice-covered nodes; absolute cryospheric mass change is ultimately constrained by the gravimetry-derived spherical harmonic solution we employ. Thus, in contrast to most conventional altimetry studies, the inversion algorithm we present does not require effective densities to be associated with rates of surface elevation change. Simply put, we use altimetry to guide the finer resolution fingerprint of mass balance underlying a coarser resolution spherical harmonic solution of absolute mass change.

2.2 Algorithm

While the inversion algorithm presented by Colgan et al. (2013) had a spatial resolution of 26 km, this resolution was acknowledged as "nominal" given that specific mass balance, or mass balance *per unit ice area*, varied over substantially greater spatial scales than mass balance *per unit area*. By introducing fractional ice coverage as the only new information to the GRACE interpretation, this previous inversion approach was only ca-

pable of constraining cryosphere-attributed mass changes to within ice-covered areas, and was not capable of distinguishing spatial heterogeneity in specific mass balance between adjacent ice containing nodes. The need for further independent information, capable of distinguishing different specific mass balances at adjacent ice-containing nodes, was identified in order to achieve "actual" 26 km resolution. The algorithm we present below addresses this need, by introducing additional information in the form of altimetry-derived ice surface elevation change rate. This additional information permits different specific mass balances to be assigned at adjacent ice-containing nodes within irregularly-shaped ice-covered areas. The ultimate hybrid mass balance product derived from this inversion is consistent with fractional ice coverage, cryosphere-attributed mass changes derived from satellite gravimetry, and ice surface elevation changes derived from altimetry.

In Colgan et al. (2013), gravimetry data are refined by introducing additional information in the form of fractional ice coverage through a Gauss–Seidel-type iterative update of a higher resolution (26 km) mass balance field ($\dot{m}$), according to:

$$\dot{m}_{ij}^{k+1} = \dot{m}_{ij}^{k} + \Delta_{ij}^{k} R_{ij}^{k} F_{ij} \quad (1)$$

where k denotes a given iteration and ij are node indices in Cartesian coordinates. The iterative update term is the product of three terms: the difference between a Gaussian smoothed version of $\dot{m}_{ij}$ and the input GRACE-derived spherical harmonic solution (Δ_{ij}^{k}), a random number from a uniform distribution between 0 and 1, which serves as a stochastic source (R_{ij}^{k}), and finally independent information in the form of fractional ice coverage (F_{ij}). The first two of these terms vary by both iteration and node, whereas the latter only varies by node. A given simulation is initialized with a random $\dot{m}_{ij}$ field, and then iteratively updated until convergence within a prescribed tolerance. In Monte Carlo fashion, a large number of simulations are performed, each of which renders a higher resolution $\dot{m}_{ij}$ field that is consistent with both gravimetry and ice extent observations. These simulations are then averaged to yield an ensemble mean field, with local uncertainty in $\dot{m}_{ij}$ derived from 1σ ensemble spread (Colgan et al., 2013).

In this study, we introduce further independent information, observed ice surface elevation change rate, by adopting a successive over relaxation (SOR)-type parameter (ω_{ij}) into the iterative update term (Kincaid, 2004):

$$\dot{m}_{ij}^{k+1} = \dot{m}_{ij}^{k} + \Delta_{ij}^{k} R_{ij}^{k} F_{ij} \omega_{ij} \tag{2}$$

When $\omega > 1$, SOR can accelerate the iterative convergence of a system of equations that approach their solution asymptotically, achieving substantial computational efficiency. In contrast, when $\omega < 1$, successive under relaxation can impart stability on the iterative convergence of potentially oscillatory systems of equations. Implementing a spatially variable ω_{ij}, rather than a scalar ω, across the inversion domain permits inverted mass changes to be preferentially weighted to nodes with relatively high ω values, in comparison to adjacent nodes with relatively low ω values. As satellite altimetry is capable of resolving localized mass loss that results from outlet glacier acceleration (e.g. Zwally et al., 2011), altimetry-derived observations of ice surface elevation change rate provide a logical source of independent information for distinguishing between different specific mass balances at adjacent ice-containing nodes. Informing ω_{ij} with observations of ice surface elevation change rate allows cryosphere-attributed mass changes to be spatially distributed in a fashion that is consistent with ice surface elevation changes.

We generate a first-order spatially variable ω_{ij} field from observed ice surface elevation change rates according to:

$$\omega_{ij} = \left| \frac{\dot{z}_{ij}}{\left(\overline{\left| \dot{z}_{ij} \right|} \right)} \right| \tag{3}$$

where $\dot{z}_{ij}$ is altimetry-derived ice surface elevation change rate. This essentially computes ω_{ij} as absolute normalized ice surface elevation change rate (Fig. 3); at a given node, ω is the local absolute ice surface elevation change rate divided by the mean of

all absolute ice surface elevation change rates across the ten sectors of interest within the inversion domain. We evaluate this SOR-type ω_{ij} parameter at all ice-containing nodes within the inversion domain. We subsequently constrain extreme values of ω_{ij}. At nodes where calculated $\omega_{ij} < 1$, we prescribe $\omega_{ij} = 1$ to prevent successive under relaxation. At the < 0.01 % of nodes where calculated $\omega_{ij} > 10$, we prescribe $\omega_{ij} = 10$. These constraints allow the ω_{ij} parameter representing relative differences in ice surface elevation change to range over an order-of-magnitude across ice-containing nodes, while still maintaining numerical stability. For example, ten times more mass change would be attributed to a node with $\omega = 10$ than a neighboring node with $\omega = 1$. Spatial gradients in ω acknowledge the reality that specific mass balance typically decreases to a minimum at the periphery of an ice mass. We similarly calculate uncertainty in this SOR-type parameter ($\delta\omega_{ij}$) as:

$$\delta\omega_{ij} = \left| \frac{\sigma\dot{z}_{ij}}{\left(\left| \dot{z}_{ij} \right| + \varepsilon \right)} \right| \omega_{ij} \tag{4}$$

where $\sigma\dot{z}_{ij}$ is the 1σ standard deviation of all observed ice surface elevation change rates within node *ij*, and ε is a small number (taken here as $0.1\,\mathrm{m\,a^{-1}}$) to maintain numerical stability where $\dot{z}_{ij} \rightarrow 0$. This essentially assumes that local uncertainty in ω_{ij} is directly proportional to local uncertainty in ice surface elevation change rate. In each simulation ω_{ij} is locally perturbed by the addition of $\delta\omega_{ij} \cdot R_{ij}$, where R_{ij} is a random number array that varies by node in each simulation.

Following Colgan et al. (2013), we invert a 1000 simulation ensemble of GRACE-derived cryosphere-attribute rates of mass change. In each simulation within the ensemble, the best estimate of the GRACE-derived spherical harmonic representation ($\dot{M}^G$) is randomly perturbed within its associated error ($\delta\dot{M}^G$), to yield a unique $\dot{M}^G + \delta\dot{M}^G$ input field. A given Monte Carlo simulation is initialized with a spatially variable $\dot{m}_{ij}$ field comprised of an array of random numbers uniformly distributed between -100 and $+100\,\mathrm{kg\,m^{-2}\,a^{-1}}$ that has been multiplied by fractional ice area (F_{ij}). This

initial $\dot{m}_{ij}$ field varies over the same order of magnitude as the anticipated final $\dot{m}_{ij}$ field, and thus minimizes hysteresis resulting from prescribed initial conditions. Beginning with the initial condition, the higher resolution (26 km) mass balance field ($\dot{m}$) is iteratively updated, substituting Eq. (2) (above) for Eq. (4) in Colgan et al. (2013), until convergence. In each iteration of each simulation the difference between the input $\dot{M}^G$ and the Gaussian-smoothed $\dot{m}$ field ($\dot{M}$) is randomly perturbed according to $\Delta^k_{ij} R^k_{ij}$ in Eq. (2). We adopt the convergence parameter and isotropic Gaussian scaling length determined by previous sensitivity analysis, 0.1 Gt a^{-1} and 200 km, respectively (Colgan et al., 2013). To summarize the multiple sources of stochasticity in the algorithm, random numbers are used to: (i) globally perturb the input GRACE-derived spherical harmonic within its associated uncertainty in each simulation, (ii) locally perturb the SOR-type introduction of surface elevation change data in each simulation, and (iii) locally perturb the update term in each iteration. This ensures that inferred mass balance is not required to be spatially correlated (e.g. subject to a covariance matrix), and enhances the algorithm's ability to efficiently explore the infinite number of possible solutions (e.g. Colgan et al., 2012).

Implementation of this SOR-type convergence acceleration, through the introduction of an altimetry-informed ω_{ij} field as described by Eqs. (3) and (4), does accelerate convergence over the comparatively implicit $\omega = 1$ approach of Colgan et al. (2013). A consequent decrease in the number of iterations required to reach convergence translates into an ~ 28 % gain in computational efficiency (Fig. 4). On high memory nodes of the University of Colorado Janus Supercomputer, a 2.8 GHz core with 12 GB of RAM solves the above system of equations with spatially variable ω to convergence in 131 ± 17 processor seconds (cf. 181 ± 17 processor seconds in an $\omega = 1$ approach; Colgan et al., 2013). Further numerical gains in computational efficiency, which would be required to perform a similar inversion over a large area like Antarctica, may be difficult to attain. At present, maintaining three-dimensional Gaussian filter weight arrays, whereby each node in two-dimensional space has a unique Gaussian filter weight array, is undoubtedly the most computationally expensive algorithm component. The

implementation of irregularly spaced grid systems, may offer the possibility to reduce the number of computation nodes by an order of magnitude (e.g. Bohlen and Saenger, 2006).

2.3 Boundaries

The inversion domain we employ is identical to that of Colgan et al. (2013). In the US National Snow and Ice Data Center (NSIDC) polar stereographic projection, the inversion domain extends from −1625 km in the west to 1300 km in the east, and from −125 km in the north to −3800 km in the south (Fig. 1). We employ a uniform grid spacing of 26 km, which results in 113 computational nodes along the Easting axis and 142 computational nodes along the Northing axis, for a total of 16 046 computational nodes within the model domain. This grid spacing resolution is the highest resolution that allows the isotropic Gaussian filter node-specific dimensionless weighting values to be stored as a single three dimensional array of $113 \times 142 \times 16\,046$ elements on the per processor RAM available on the University of Colorado's Janus Supercomputer. The polar stereographic projection inherently introduces increasing distortion away from its central meridian (45° W) and parallel (70° N), which influences area calculations. We compensate for area distortion by calculating the true area of each individual node across the domain (A_{ij}). The true areas of ice-containing nodes vary between 24.5^2 and 27.5^2 km^2 over the domain.

By employing a spherical harmonic representation of cryosphere-attributed mass change ($\dot{M}^G$), the mass balances associated with non-ice containing nodes are theoretically negligible (e.g. $\dot{m} = 0\,\mathrm{kg\,m^{-2}\,a^{-1}}$ where $F = 0$). Practically, however, mass balances at non-ice containing nodes are not truly zero, but rather within uncertainty of zero (e.g. $\dot{m} \approx 0\,\mathrm{kg\,m^{-2}\,a^{-1}}$ where $F = 0$). Following a sensitivity study by Colgan et al. (2013), we prescribe a non-ice containing node absolute threshold ($\dot{m}_{\max}$) of $15\,\mathrm{kg\,m^{-2}\,a^{-1}}$. Simply put, this permits the inversion to assign between −15 and $+15\,\mathrm{kg\,m^{-2}\,a^{-1}}$ of mass change at non-ice containing nodes. The level of mass change

uncertainty at non-ice containing nodes acknowledged by this boundary condition is representative of the level of uncertainty typically assessed for GRACE-derived cryosphere-attributed spherical harmonic solutions (e.g. Velicogna and Wahr, 2005; Longuevergne et al., 2010), and an order of magnitude less than the $\dot{m}_{ij}$ values inferred by the inversion at adjacent ice-containing nodes. This boundary condition is implemented at non-ice containing nodes according to a Heaviside, or logic, function invoked to appropriately modify Eq. (2) where $F = 0$ (Eqs. 6 and 7 in Colgan et al., 2013).

3 Results

In comparison to the gravimetry-inversion mass balance product presented by Colgan et al. (2013), which does not include altimetry-derived information on the relative ice surface elevation changes at adjacent nodes, the HIGA mass balance product assigns more mass loss at Greenland tidewater outlet glaciers, where relatively rapid dynamic drawdown is occurring, which is offset by less mass loss assigned further inland on the ice sheet (Fig. 5). This effectively results in a higher mass balance gradient with distance inland or elevation. Changes in specific mass balance between these two inversion approaches are negligible in both the ice sheet interior, where relative differences in surface elevation changes between adjacent nodes become small, and at non-ice containing nodes, where mass changes are constrained by boundary conditions. As the HIGA mass balance product assigns mass balance as proportional to relative period trends in ice surface elevation rate, it yields a spatially heterogeneous specific mass balance field (i.e. *per unit ice area*), rather than one with gentle spatial gradients across ice-covered areas (cf. Fig. 13 of Colgan et al., 2013). Given the ability of an iterative inversion to constrain GRACE-derived mass changes within irregularly-shaped ice-covered areas, and the inclusion of altimetry-derived surface elevation changes to differentiate rates of mass change between adjacent nodes, HIGA $\dot{m}$ values are expected to be accurate at 26 km actual resolution within the local uncertainty defined by

ensemble spread (Fig. 6). In Sect. 4.1, we attempt to validate HIGA $\dot{m}$ values against in situ $\dot{m}$ observations. We note that the estimates of cryosphere-attributed mass change we present are dependent on the GRACE-derived spherical harmonic representation employed as algorithm input.

Over the IMBIE period, the HIGA inversion suggests that the Greenland Ice Sheet proper was responsible for $217 \pm 20\,\mathrm{Gt\,a^{-1}}$ of mass loss (cf. $218 \pm 20\,\mathrm{Gt\,a^{-1}}$; Colgan et al., 2013). This is significantly less ($\sim 17\,\%$) than the ice sheet mass loss assessed by the IMBIE ($263 \pm 30\,\mathrm{Gt\,a^{-1}}$; Shepherd et al., 2012). We note, however, that the IMBIE grouped both peripheral glaciers and the ice sheet proper into a single Greenland mass loss value. Accounting for the additional mass loss of $38 \pm 6\,\mathrm{Gt\,a^{-1}}$ that we attribute to Greenland peripheral glaciers over the period, brings our estimates of total Greenland mass loss within error of the IMBIE value (Table 1). The peripheral glacier mass loss of $50 \pm 8\,\mathrm{Gt\,a^{-1}}$ that we attribute to the Canadian Arctic (Sectors 9 and 10) is greater than the analogous $33 \pm 22\,\mathrm{Gt\,a^{-1}}$ over the March 2003 to February 2010 period assessed by Schrama and Wouters (2011) using gravimetry, and less than the reconciled altimetry and gravimetry estimate of $60 \pm 8\,\mathrm{Gt\,a^{-1}}$ over the October 2003 to October 2009 period assessed by Gardner et al. (2013). We note that our Canadian Arctic mass loss estimate is within overlapping uncertainty of both these previously published values. Spatially variable tuning of the SOR-type ω_{ij} parameter may provide a means to reduce spatial discrepancies, but we elect to maintain our HIGA product as completely untuned and consistent with Greenland IMBIE results.

Of the ten geographic sectors we examine across Greenland and the Canadian Arctic, only one (Sector 2 in Northeast Greenland) is within error of zero balance. The remaining nine sectors are in negative balance, resulting in a total ice loss of $316 \pm 37\,\mathrm{Gt\,a^{-1}}$ across the study area over the IMBIE period. Peripheral glaciers in both Greenland and the Canadian Arctic account for $88 \pm 14\,\mathrm{Gt\,a^{-1}}$ (or $\sim 28\,\%$) of this mass loss. Within Greenland, peripheral glaciers contribute the greatest mass loss in Sector 3 ($11 \pm 2\,\mathrm{Gt\,a^{-1}}$), which includes the abundant peripheral glaciers of the Geikie Plateau, and the least mass loss in Sector 2 ($0 \pm 0\,\mathrm{Gt\,a^{-1}}$), which is in the relatively arid North-

east Greenland. Mass loss from the ice sheet proper is greatest in Sectors 8 (Northwest Greenland) and 3 (East Greenland), where large tidewater glaciers are present, and least in Sector 1 (North Greenland), which is predominately land terminating. We note that while Sector 6 (Southwest Greenland) has relatively few tidewater glaciers, it has a greater mass loss than comparably-sized Sector 4 (Southeast Greenland) and Jakobshavn (Sector 7), both of which have appreciable numbers of tidewater glaciers. HIGA specific $\dot{m}$ values (i.e. *per unit ice area*) reach a minimum of $-4.2\,\mathrm{m\,WE\,a^{-1}}$ near the terminus of Jakobshavn Isbrae, and a maximum of $0.9\,\mathrm{m\,WE\,a^{-1}}$ on the southern tip of Baffin Island. Following Colgan et al. (2013), we attribute this pocket of anomalous positive values on Baffin Island to the inability of the inversion to satisfy anomalously high oceanic mass gain within the parameter space we employ (e.g. characteristic Gaussian filter length scale and absolute threshold of non-ice containing nodes). This may reflect unidentified oceanic mass changes that are not captured in the forward ocean model used to isolate cryospheric mass loss, and note that gravimetry signal leakage is greatest where cryospheric mascons are surrounded by non-cryospheric mascons on three sides.

4 Discussion

4.1 Comparison with in situ observations

Here, we compare local HIGA $\dot{m}$ values with all available in situ $\dot{m}$ observations within our inversion domain. We believe this is the first time a GRACE-derived product has been directly compared with point measurements of mass balance. We consider in situ $\dot{m}$ measurements made via three techniques: (i) the "coffee can" approach, (ii) the surface mass balance and strain network method and (iii) repeat geodetic survey with volume-to-mass conversion. The "coffee can" method, pioneered by Hamilton et al. (1998) and named after coffee cans deployed in boreholes, calculates change in water-equivalent (WE) thickness as the sum of long term surface mass balance, vertical

ice velocity, and a correction for subtle downslope movement of the coffee can during the measurement period. The unique aspect of this approach is correcting observed snow surface vertical velocity with a direct measurement of the rate of firn densification, in order to isolate vertical ice velocity at the firn–ice interface. Firn densification rate is assessed through repeat measure of the distance between a coffee can anchored at depth and a given annual surface above (Hamilton et al., 1998). Coffee can-derived $\dot{m}$ observations have been made at several sites on the Greenland Ice Sheet, as well as on the Devon Ice Cap (Hamilton and Whillans, 2002; Burgess et al., 2008). As $\dot{m}$ is essentially derived by differencing long term ice dynamics and long term surface mass balance, the resultant $\dot{m}$ values reflect mass balance for the past several decades leading up to the measurement period. Therefore, coffee can-derived $\dot{m}$ values should only be compared to HIGA-inferred $\dot{m}$ values with the knowledge that the latter reflects the 2004 to 2010 IMBIE period, while the former reflects a longer multi-decadal period.

The second method uses measurements of surface strain and surface mass balance to derives in situ $\dot{m}$ by differencing long term ice dynamics and long term surface mass balance. Rather than attempting to measure a densification-corrected vertical ice velocity, however, this approach relies on combining observations of local strain rates, both parallel and perpendicular to ice flow, with knowledge of ice thickness in order to assess vertical ice velocity via mass continuity (Reeh and Gundestrup, 1985; Burgess and Sharp, 2008). Thus, similar to the coffee can method, strain-derived $\dot{m}$ values are not directly comparable to HIGA values, as they reflect mean mass balance over the past several decades, rather the precise 2004 to 2010 IMBIE period. Within our inversion domain, strain-derived $\dot{m}$ values are available at Dye-3 and the Devon Ice Cap (Reeh and Gundestrup, 1985; Burgess and Sharp, 2008). Although not directly comparable, we still include both coffee can and strain-derived multi-decadal $\dot{m}$ values in our validation assessment, if only to demonstrate that 26 km spatial resolution HIGA $\dot{m}$ values are reasonable.

The third method for measuring $\dot{m}$ in situ is through repeat geodetic ground surveys, in which changes in surface elevation are combined with associated density to estimate

mass balance (Stober et al., 2013). Unlike the other two in situ $\dot{m}$ methods, neither long term ice dynamic nor long term surface mass balance are invoked in the geodetic method, which means that HIGA-inferred $\dot{m}$ values are directly comparable to geodetic-derived $\dot{m}$ values observed over the same period. Geodetic-derived $\dot{m}$ values have been observed over the IMBIE period, or within a few years of the IMBIE period, at both Swiss Camp and the Ohio State University (OSU) clusters in Greenland (Jezek, 2011; Stober et al., 2013). In the ablation region, where geodetic measurements are made on snow-free (bare) ice, the effective density of change can be assumed as the density of ice (e.g. Swiss Camp). In the accumulation region, where a snow pack or firn column exists, observations of surface elevation must be accompanied by observations of near surface density and rate of change of near surface density (e.g. OSU clusters).

The mass of a given ice column (m) may be described as the product of its mean density (ρ) and thickness (H):

$$m = \rho H \tag{5}$$

Given that both density and thickness are dependent on time (e.g. $\rho(t)$ and $H(t)$), it follows from the Leibniz or product rule that the transient rate of mass change of a given ice column ($\dot{m}$) may be described as:

$$\dot{m} = \rho\dot{H} + \dot{\rho}H \tag{6}$$

where the first term can be interpreted as describing mass change due to ice thickness change of known density, and the second term can be interpreted as describing mass change due to firn density change of known thickness. Fortunately, both firn cores and firn density modelling provide insight on the rate of change in firn density ($\dot{\rho}$) at the OSU central cluster, high in the South Greenland accumulation zone. Near surface (15 m deep) density profiles from the OSU central cluster suggest $\dot{\rho} = -3.8\,\mathrm{kg\,m^{-3}\,a^{-1}}$ over the 1981 to 1993 period (Jezek, 2012). Over the 2003 to 2007 period, firn modeling suggests a slight densification of $83\,\mathrm{kg\,m^{-2}\,a^{-1}}$, equivalent to $\dot{\rho} = +5.5\,\mathrm{kg\,m^{-3}\,a^{-1}}$ if distributed over a 15 m firn column (Zwally et al., 2011). Jezek (2011) suggests that the

changes in ice sheet elevation observed at the OSU clusters are most consistent with independent flux-gate estimations of mass change when the effective density of elevation change is taken as ice density, and thus when changes in near-surface density are assumed to be small (e.g. $\dot{\rho} \approx 0$). We therefore assume $\dot{\rho} = 0 \pm 5\,\mathrm{kg\,m^{-3}\,a^{-1}}$ when converting observations of surface elevation change into total mass balance at the OSU clusters. This uncertainty approximates the range of contrasting firn densification rates derived from in situ and model approaches.

After reviewing the glaciology literature, we find 23 previously published point measurements of in situ mass balance across the Canadian Arctic and Greenland (Table 2). We compare these in situ observations to the specific mass balance (i.e. *per unit ice area*) inferred from our HIGA product, which is calculated as mass balance (i.e. *per unit area*) divided by fractional ice coverage (Fig. 7; Colgan et al., 2013). Of these 23 sites, there are only four sites at which the majority of the in situ observation period falls within the IMBIE period. At three of these four sites (OSU West, OSU Central and Swiss Camp) the HIGA $\dot{m}$ is within error of $y = x$ (Fig. 8). HIGA $\dot{m}$ appears to overestimate observed mass loss at ST2, beyond the uncertainty approximated by local ensemble spread. We note that as spatial heterogeneity in mass balance increases towards the ice sheet margin, a point measurement of $\dot{m}$ is less likely to be representative of a larger area (e.g. 26 by 26 km) in comparison to the ice sheet interior. Although the $\dot{m}$ values observed at the remaining 19 sites are not directly comparable to HIGA $\dot{m}$ values due to substantial differences in observation periods, HIGA $\dot{m}$ is still within error of $y = x$ at the majority of these sites. The majority of historical $\dot{m}$ observations lie beneath $y = x$, which is consistent with the notion that mass balance has generally decreased since these historical observation periods. For the four sites with a time span consistent with the IMBIE period, the root mean squared difference (RMSD) between in situ and HIGA $\dot{m}$ is $0.18\,\mathrm{m\,WE\,a^{-1}}$. The small sample size prevents this RMSD from serving as an independent assessment of the absolute accuracy of HIGA-inferred $\dot{m}$. Instead, we suggest that this validation exercise only qualitatively demonstrates that completely untuned HIGA $\dot{m}$ values compare well to observations where available.

The overarching message of our validation attempt is that there is an urgent need for in situ mass balance measurements in order to calibrate and validate higher resolution remotely sensed mass balance products. Presently, the only four sites available for direct comparison during the IMBIE period all lie south of 70° N on the Greenland Ice Sheet proper. These in situ observations sample neither regions of high mass loss, where dynamic drawdown rates can exceed > 2 m WE a^{-1}, nor peripheral ice caps and glaciers, which comprise ∼ 15 % of Greenland's mass loss (Bolch et al., 2013; Colgan et al., 2013). Given the decadal-scale temporal resolution of both coffee can and strain network approaches, it may be possible to collect in situ observations in the near future that have validation utility for the (now historic) IMBIE period. For example, combining observed strain rates recovered in 2015 with 15 yr mean surface balance data would essentially produce an $\dot{m}$ estimate for the 2000 to 2015 period, which closely approximates the anticipated GRACE mission duration. While this would only be possible at sites with appropriate dynamic response timescales, this could greatly improve the inventory of in situ $\dot{m}$ values available for validating both current and future higher resolution satellite gravimetry-derived mass balance products.

4.2 Spatial partition of the continuity equation

The mass balance ($\dot{m}$) at any point on a glacier is the difference between surface mass balance ($\dot{b}$) and the horizontal divergence of ice flux (∇Q), as described by the transient glacier continuity equation:

$$\dot{m} = \dot{b} - \nabla Q \tag{7}$$

Differencing HIGA $\dot{m}$ with an independent estimate of surface mass balance allows the ice dynamic portion of mass balance to be solved as a residual (Fig. 9). We employ modelled $\dot{b}$ over the IMBIE period (2004 to 2010) from the regional climate model MAR (version 3.2) forced with ERA-Interim reanalysis data along the boundary of the model domain (Fettweis et al., 2013). While this MAR-derived $\dot{b}$ field is available over all of Greenland at 25 km resolution, it does not extend over the Canadian Arctic. Following

the identification of an accumulation bias in MAR (version 2.1), which resulted in an RMSE of 46 % (24 %) with local $\dot{b}$ observations above (below) 1500 m elevation (Vernon et al., 2013), MAR (version 3.2) has been tuned with 86 spatially distributed ice core-derived accumulation records (Box et al., 2013). MAR (version 3.2) reproduces local surface mass balance observations with an RMSE of ∼ 20 %, and ice sheet wide net surface mass balance with an uncertainty of ∼ 10 % (Fettweis et al., 2013). Thus, for the purposes of partitioning the transient continuity equation at 26 km resolution, we take uncertainty in local MAR (version 3.2) $\dot{b}$ as ±20 %. Solving ∇Q as a residual inherently compounds the uncertainties in both $\dot{b}$ and $\dot{m}$, which we assume sum quadratically. Given the difficulties associated with assessing contemporary ∇Q either from first principles numerical modelling or remotely sensed observations, we suggest that there is value in solving transient ∇Q as a residual, despite the relatively high consequent uncertainty, which approaches 1 m WE a^{-1} near the terminus of Jakobshavn Isbrae (Fig. 10).

The residual ∇Q field generally exhibits divergence of horizontal flux throughout the ice sheet interior (e.g. $-\nabla Q$) and convergence of horizontal flux (e.g. $+\nabla Q$) around the ice sheet periphery (Fig. 9). This is consistent with negative (submerging) vertical ice velocities in the ice sheet accumulation region, and positive (emerging) vertical ice velocities in the ice sheet ablation region. Closer inspection, however, reveals contrasting ice dynamic signatures of predominately marine-terminating portions of the ice sheet (e.g. Southeast Greenland and Geikie Plateau) and predominately land-terminating portions of the ice sheet (e.g. North Greenland and Southwest Greenland). In land-terminating regions there is a wide band of convergent (or emergent) ice flux along the ice sheet periphery, while in marine-terminating regions the ice flux is divergent (or submergent) along the ice sheet periphery. We discuss an anomalous small region of convergent ice flux in north central Greenland, where divergent ice flux would normally be expected, in Sect. 4.3.

We compare IMBIE period residual ∇Q values at 26 km resolution with historical (c. 1950 to 2000) in situ point measurements of vertical ice velocity at ten higher elevation

sites on the Greenland Ice Sheet (Hamilton and Whillans, 2002), and find that only half are within error of $y = x$ (Fig. 11). Implicit in this comparison is the assumption that any changes in ice velocity at high elevation between the c.1950 to 2000 period and the IMBIE period are negligible (Joughin et al., 2010). Residual ∇Q values systematically underestimate in situ vertical velocities at all but one site (NASA-E). Assuming this discrepancy can be explained by a combination of both MAR model or HIGA algorithm error, this systematic bias towards less horizontal divergence of ice flux than historically observed may stem from either HIGA-inferred $\dot{m}$ systematically overestimating true $\dot{m}$, or MAR-derived $\dot{b}$ systematically underestimating true $\dot{b}$ (Fig. 8). By virtue of solving ∇Q as a residual, any overestimation (underestimation) of $\dot{m}$ ($\dot{b}$) results in a direct underestimation of ∇Q (Eq. 7). Given a historical MAR bias towards overestimating accumulation in the ice sheet interior (Vernon et al., 2013), we speculate that our apparent underestimation of residual ∇Q more likely stems from overestimated HIGA-inferred $\dot{m}$ than underestimated MAR-modeled $\dot{b}$. We note, however, that aggregated across the high elevation ice sheet interior, which we take as the area enclosed by the 2000 m elevation contour, HIGA-inferred $\dot{m}$ suggests a mass balance of 10 ± 4 Gt a^{-1} during the IMBIE period. This slightly positive high elevation mass balance, equivalent to ~ 1 cm WE a^{-1} ice thickening, is consistent with in situ observations that the high elevation region is close to zero balance (Thomas et al., 2001).

4.3 Millennial scale ice dynamics

The Greenland Ice Sheet is assumed to have been in near equilibrium during the 1961 to 1990 reference period (van den Broeke et al., 2009). The residual ∇Q field we present here, however, suggests that ice dynamics may be contributing to a substantial mass gain in the ice sheet interior (Fig. 9). This is especially evident in a region of convergent ice flux in north central Greenland, where divergent ice flux would normally be expected. Simply put, HIGA-inferred $\dot{m}$ assigns more mass gain to this region than could be explained by $\dot{b}$ in the absence of any ice flow (i.e. $\dot{m} > \dot{b}$). While this underestimation of residual flux divergence most likely results from overestimated HIGA-

inferred $\dot{m}$, we note that this apparent artifact is consistent with the magnitude and spatial distribution of subtle mass gain anticipated from millennial scale ice dynamics. Transient mass gain associated with ice dynamics is expected to be most evident near flow divides in north central Greenland due to: (i) nearly vertical ice flow, which makes changes in ice surface elevation due to ice dynamics more pronounced than areas where ice flow approaches surface-parallel, and (ii) relatively low accumulation rates, which amplifies a given anomaly in ice dynamics in comparison to higher accumulation sites.

The Greenland Ice Sheet is estimated to have been ~ 15 % thinner than present during the peak of the Wisconsin glaciation ~ 21 kaBP, due to the smaller crystal size and increased solute concentration of Wisconsin ice in comparison to Holocene ice (Reeh, 1985). Consequently, the ice sheet is hypothesized to be presently undergoing a subtle high elevation thickening due to the gradual replacement of softer Wisconsin ice with firmer (or more viscous) Holocene ice. Potentially analogous long term dynamic ice cap thickening has been observed in the Canadian Arctic (Colgan et al., 2008). In Greenland, this subtle high elevation thickening has a hypothesized rate of ~ 1 cm WE a^{-1} (Reeh, 1985), which is corroborated by coarse resolution (20 km) 3-D thermo-mechanical ice flow modelling (Huybrechts, 1994). Reeh and Gundestrup (1985) explicitly attribute an in situ mass balance of 3 ± 6 cm WE a^{-1} observed at Dye-3 to millennial-scale ice dynamics associated with the Wisconsin-Holocene transition. At seven additional widely distributed high elevation sites (South Dome, Saddle, Dye-2, Summit, NASA-E, Camp Century and Humboldt), which are unlikely to be influenced by enhanced flow mechanisms (i.e. surface velocity < 27 m a^{-1}), in situ coffee can measurements similarly identify a mean thickening of 3 ± 12 cm WE a^{-1}, including an observation of net thinning at Camp Century (Hamilton and Whillans, 2002).

Applying a secular mass gain signal of ~ 2 cm WE a^{-1} across the high elevation ice sheet region delineated by the Program for Arctic Regional Climate Assessment (PARCA; Thomas et al., 2001) changes the majority of the slightly convergent ice flux values in north central Greenland (e.g. $-$ve ∇Q) into slightly divergent ice flux values

(e.g. +ve ∇Q), and thus improves notional consistency with radial flow extending downwards from the local flow divides (Fig. 12). Application of a secular thickening trend also acts in favour of reducing the discrepancy between residual ∇Q and in situ vertical ice velocities at sites above the PARCA perimeter (Fig. 11). This secular mass gain trend is within the range of theoretical, modelled and observed thickening trends attributed to the ongoing Wisconsin-Holocene transition (Reeh, 1985; Reeh and Gundestrup, 1985; Huybrechts, 1994; Hamilton and Whillans, 2002). In order to explicitly acknowledge the role of millennial scale ice dynamics when spatially partitioning the transient glacier continuity equation, shorter term (ST) and longer term (LT) ice dynamics may be conceptualized as:

$$\dot{m} = \dot{b} - \nabla Q_{\mathrm{ST}} - \nabla Q_{\mathrm{LT}} \quad (8)$$

where centurial to millennial scale dynamic mass changes occurring during reference period are attributed to longer term ice dynamics (∇Q_{LT}), and annual to decadal scale dynamic mass changes occurring since reference period are attributed to shorter term ice dynamics (∇Q_{ST}; Fig. 12).

While acknowledging the role of subtle millennial scale high elevation thickening may be important in achieving a spatial partition of $\dot{b}$ and ∇Q that is theoretically consistent with the transient glacier continuity equation, it challenges the assumption that the Greenland Ice Sheet was in near-equilibrium during the recent 1961 to 1990 reference climatology period (cf. van den Broeke et al., 2009). A thickening rate of $2\,\mathrm{cm\,WE\,a^{-1}}$ distributed uniformly across the $9.8 \times 10^5\,\mathrm{km^2}$ of ice sheet area above the nominal 2000 m elevation PARCA perimeter is equivalent to an annual mass gain of ~ 18 Gt. While this signal is within error of estimates of ice sheet scale annual accumulation or iceberg calving, it is non-trivial ($\sim 8\,\%$) and opposite in sign in comparison to recent ice sheet mass balance, which we assess as $-217\,\mathrm{Gt\,a^{-1}}$. We acknowledge, however, that the formal uncertainty associated with local residual ∇Q values we assess in north central Greenland ($\sim 10\,\mathrm{cm\,WE\,a^{-1}}$) is substantially larger than the speculated thickening signal we attribute to the ongoing Wisconsin-Holocene transition. Invoking Occam's razor (e.g. Anderson, 2002), an overestimation of HIGA $\dot{m}$ is the most likely explanation for our systematic underestimation of residual ∇Q values; the consistency of our apparent ∇Q artifact with the magnitude and spatial distribution of subtle mass gain anticipated from millennial scale ice dynamics is curious, but likely entirely coincidental. A thorough understanding of high elevation mass balance during the 1961 to 1990 reference climatology period, however, to verify $\nabla Q_{\mathrm{LT}} \approx 0$, is required before excluding millennial scale ice dynamics as a factor in contemporary high elevation mass balance.

5 Summary remarks

The mass balance product that we derive through iterative inversion is simultaneously consistent with glacier inventory, cryosphere-attributed mass changes derived from satellite gravimetry, and ice surface elevation changes derived from airborne and satellite altimetry. This HIGA product combines the complementary strengths of gravimetry and altimetry to refine direct measurements of cryosphere-attributed mass change to relatively high spatial resolution. While we have attempted to validate HIGA mass balance values against in situ observations, we find only a handful of locations throughout Greenland and the Canadian Arctic where mass balance was measured over a time period directly comparable to the IMBIE period (2004 to 2010). We therefore identify an urgent need for additional in situ measurements of mass balance to calibrate higher resolution remotely sensed mass balance products.

Of the $316 \pm 37\,\mathrm{Gt\,a^{-1}}$ of mass loss over the Canadian Arctic and Greenland during the IMBIE period, we attribute $217 \pm 20\ \mathrm{Gt\,a^{-1}}$ to the ice sheet proper, and 38 ± 6 $\mathrm{Gt\,a^{-1}}$ and $50 \pm 8\,\mathrm{Gt\,a^{-1}}$ to peripheral glaciers in Greenland and the Canadian Arctic, respectively. We note that these mass loss estimates are dependent on the spherical harmonic representation with which we initialized our iterative inversion. Employing a different spherical harmonic representation would be expected to produce different mass loss estimates. The mass losses we assess in Greenland are consistent with

previously published estimates, while the mass loss we assess to the Canadian Arctic is within overlapping uncertainties of previously published estimates. Given that Greenland's peripheral glaciers, which comprise < 5 % of Greenland's ice covered area, appear to be contributing ∼ 15 % of the aggregate Greenland mass loss observed by satellite gravimetry, GRACE-derived estimates of "Greenland" mass loss cannot reasonably be taken as synonymous with "Greenland ice sheet" mass loss. Comparisons of GRACE-derived mass loss should therefore be limited to other mass balance techniques (i.e. input-output or altimetry) that sample both the ice sheet and its peripheral glaciers.

Combining HIGA mass balance with surface mass balance from the regional climate model MAR has allowed us to solve the transient glacier continuity equation at 26 km resolution across Greenland during the December 2003 to December 2010 period. The residual horizontal divergence of flux field (∇Q) is generally consistent with the notion of divergent ice flow (submergent velocities) in the ice sheet accumulation region and convergent ice flow (emergent velocities) in land-terminating ablation regions. Marginal areas with divergent ice flow generally correspond to regions of marine-terminating glaciers, consistent with a dynamic mass loss mechanism. This first-order partition of the transient continuity equation, however, infers a small pocket of convergent ice flow in North Central Greenland, which is not consistent with theoretical and observed radial flow ice velocities. We speculate that a systematic underestimation of observed vertical ice velocities stems from an overestimation of HIGA-inferred mass balance in the ice sheet interior. We note, however, that this apparent artifact in the flux divergence field is consistent in magnitude and spatial distribution with subtle high elevation mass gain, which has been previously postulated in association with the downward advection of the Wisconsin-Holocene transition within the ice sheet.

Supplementary material related to this article is available online at http://www.the-cryosphere-discuss.net/8/537/2014/tcd-8-537-2014-supplement.zip.

Acknowledgements. This work was funded by NASA award NNX10AR76G and DFF award FNU 11-115166. This work utilized the Janus supercomputer, which is supported by NSF award CNS-0821794 and the University of Colorado Boulder. The Janus supercomputer is a joint effort of the University of Colorado Boulder, the University of Colorado Denver and the National Center for Atmospheric Research. W. C. thanks Joel Frahm for his continued assistance working with Janus. M. C. was supported by PROMICE and GlacioBasis with funds from the Danish Energy Agency. We thank Ken Jezek very much for sharing his field data and reviewing our interpretation of the mass balance of the Ohio State University clusters in South Greenland.

References

Alley, R., Spencer, M., and Anandakrishnan, S.: Ice-sheet mass balance: assessment, attribution, and prognosis, Ann. Glaciol., 46, 1–7, 2007.

Anderson, D.: Occam's Razor: simplicity, complexity„ and global geodynamics, P. Am. Philos. Soc., 146, 56–70, 2002.

Arendt, A., Bolch, T., Cogley, J., Gardner, A., Hagen, J., Hock, R., Kaser, G., Pfeffer, W., Moholdt, G., Paul, F., Radic, V., Andreassen, L., Bajracharya, S., Beedle, M., Berthier, E., Bhambri, R., Bliss, A., Brown, I., Burgess, E., Burgess, D., Cawkwell, F., Chinn, T., Copland, L., Davies, B., De Angelis, H., Dolgova, E., Filbert, K., Forester, R., Fountain, A., Frey, H., Giffen, B., Glasser, N., Gurney, S., Hagg, W., Hall, D., Haritashya, U., Hartmann, G., Helm, C., Herreid, S., Howat, I., Kapustin, G., Khromova, T., Kienholz, C., Koenig, M., Kohler, J., Kriegel, D., Kutuzov, S., Lavrentiev, I., LeBris, R., Lund, J., Manley, W., Mayer, C., Miles, E., Li, X., Menounos, B., Mercer, A., Moelg, N., Mool, P., Nosenko, G., Negrete, A., Nuth, C., Pettersson, R., and Racoviteanu, A.: Randolph Glacier Inventory version 2.0: A Dataset of Global Glacier Outlines, Global Land Ice Measurements from Space, Digital Media, Boulder Colorado, USA, 2012.

Bohlen, T. and Saenger, E.: Accuracy of heterogeneous staggered-grid finite-difference modeling of Rayleigh waves, Geophysics, 71, T109–T115, 2006.

Bolch, T., Sandberg Sørensen, L., Simonsen, S., Mölg, N., Machguth, H., Rastner, P., and Paul, F.: Mass loss of Greenland's glaciers, and ice caps 2003–2008 revealed from ICESat laser altimetry data, Geophys. Res. Lett., 40, 875–881, doi:10.1002/grl.50270, 2013.

Borsa, A. A., Moholdt, G., Fricker, H. A., and Brunt, K. M.: A range correction for ICESat and its potential impact on ice sheet mass balance studies, The Cryosphere Discuss., 7, 4287–4319, doi:10.5194/tcd-7-4287-2013, 2013.

Box, J., Cressie, N., Bromwich, D., Jung, J., van den Broeke, M., van Angelen, J., Forster, R., Miege, C., Mosley-Thompson, E., Vinther, B., and McConnell, J.: Greenland ice sheet mass balance reconstruction, Part I: net snow accumulation (1600–2009), J. Climate, 26, 3919–3934, 2013.

Burgess, D. and Sharp, M.: Recent changes in thickness of the Devon Island ice cap, Canada, J. Geophys. Res., 113, B07204, doi:10.1029/2007JB005238, 2008.

Chao, B., O'Connor, W., Chang, A., Hall, D., and Foster, J.: Snow load effect on the Earth's rotation, and gravitational field, 1979–1985, J. Geophys. Res., 92, 9415–9422, 1987.

Citterio, M. and Ahlstrøm, A. P.: *Brief communication* "The aerophotogrammetric map of Greenland ice masses", The Cryosphere, 7, 445–449, doi:10.5194/tc-7-445-2013, 2013.

Colgan, W., Davis, J., and Sharp, M.: Is the high-elevation region of Devon Ice Cap thickening?, J. Glaciol., 54, 428–436, 2008.

Colgan, W., Pfeffer, W. T., Rajaram, H., Abdalati, W., and Balog, J.: Monte Carlo ice flow modeling projects a new stable configuration for Columbia Glacier, Alaska, c. 2020, The Cryosphere, 6, 1395–1409, doi:10.5194/tc-6-1395-2012, 2012.

Colgan, W., Luthcke, S., Abdalati, W., and Citterio, M.: Constraining GRACE-derived cryosphere-attributed signal to irregularly shaped ice-covered areas, The Cryosphere, 7, 1901–1914, doi:10.5194/tc-7-1901-2013, 2013.

Ek, M., Mitchell, K., Lin, Y., Rogers, E., Grunmann, P., Koren, V., Gayno, G., and Tarpley, J.: Implementation of Noah land surface model advances in the National Centers for Environmental Prediction operational mesoscale Eta model, J. Geophys. Res., 108, 8851, doi:10.1029/2002JD003296, 2003.

Fettweis, X., Franco, B., Tedesco, M., van Angelen, J. H., Lenaerts, J. T. M., van den Broeke, M. R., and Gallée, H.: Estimating the Greenland ice sheet surface mass balance contribution to future sea level rise using the regional atmospheric climate model MAR, The Cryosphere, 7, 469–489, doi:10.5194/tc-7-469-2013, 2013.

Fricker, H., Borsa, A., Minster, B., Carabajal, C., Quinn, K. K., and Bills, B.: Assessment of ICESat performance at the Salar de Uyuni, Bolivia, Geophys. Res. Lett., 32, L21S06, doi:10.1029/2005GL023423, 2005.

Gardner, A., Moholdt, G., Wouters, B., Wolken, G., Burgess, D., Sharp, M., Cogley, J., Braun, C., and Labine, C.: Sharply increased mass loss from glaciers, and ice caps in the Canadian Arctic Archipelago, Nature, 473, 357–360, doi:10.1038/nature10089, 2011.

Hamilton, G. and Whillans, I.: Local rates of ice-sheet thickness change in Greenland, Ann. Glaciol., 35, 79–83, 2002.

Hamilton, G., Whillans, I., and Morgan, P.: First point measurements of ice-sheet thickness change in Antarctica, Ann. Glaciol., 27, 125–129, 1998.

Huybrechts, P.: The present evolution of the Greenland ice sheet: an assessment by modelling, Global Planet. Change, 9, 39–51, 1994.

Jezek, K.: Surface elevation, and velocity changes on the south-central Greenland ice sheet: 1980–2011, J. Glaciol., 58, 1201–1211, 2011.

Jezek, K.: Surface Elevation, and Velocity Changes on the South Central Greenland Ice Sheet: 1980–2011 Data Summary, BPRC Technical Report No. 2012–01, Byrd Polar Res. Center, The Ohio State University, Columbus, Ohio, 28 pp. plus data summary, 2012.

Joughin, I., Smith, B., Howat, I., Scambos, T., and Moon, T.: Greenland flow variability from ice-sheet-wide velocity mapping, J. Glaciol., 56, 415–430, 2010.

Kincaid, D.: Celebrating Fifty Years of David M. Young's Successive Overrelaxation Method, Numerical Mathematics, and Advanced Applications, editd by: Feistauer, M., Dolejsi, V., Knoblock, P., and Najzar, K., Springer Berlin Heidelberg, 549–558, doi:10.1007/978-3-642-18775-9, 2004.

Li, J. and Zwally, H.: Modeling of firn compaction for estimating ice-sheet mass change from observed ice-sheet elevation change, Ann. Glaciol., 52, 1–7, 2011.

Longuevergne, L., Scanlon, B., and Wilson, C.: GRACE Hydrological estimates for small basins: evaluating processing approaches on the High Plains Aquifer, USA, Water Resour. Res., 46, W11517, doi:10.1029/2009WR008564, 2010.

Luthcke, S., Sabaka, T., Loomis, B., Arendt, A., McCarthy, J., and Camp, J.: Antarctica, Greenland, and Gulf of Alaska land-ice evolution from an iterated GRACE global mascon solution, J. Glaciol., 59, 613–631, doi:10.3189/2013JoG12J147, 2013.

Peltier, W.: Global glacial isostatic adjustment, and the surface of the ice-age Earth: the ICE-5G(VM2) model, and GRACE, Annual Reviews Earth Planetary Science, 32, 111–149, doi:10.1146/annurev.earth.32.082503.144359, 2004.

Rastner, P., Bolch, T., Mölg, N., Machguth, H., Le Bris, R., and Paul, F.: The first complete inventory of the local glaciers and ice caps on Greenland, The Cryosphere, 6, 1483–1495, doi:10.5194/tc-6-1483-2012, 2012.

Ray, R.: A global ocean tide model from TOPEX/Poseidon altimetry/GOT99.2, NASA Tech. Rep. NASA/TM-1999-209478, NASA Goddard Space Flight Center, Greenbelt, MD, 1999.

Ray, R. D. and Ponte, R. M.: Barometric tides from ECMWF operational analyses, Ann. Geophys., 21, 1897–1910, doi:10.5194/angeo-21-1897-2003, 2003.

Reeh, N.: Was the Greenland ice sheet thinner in the late Wisconsinan than now?, Nature, 317, 797–799, 1985.

Reeh, N. and Gundestrup, N.: Mass balance of the Greenland Ice Sheet at Dye-3, J. Glaciol., 31, 198–200, 1985.

Rignot, E., Box, J., Burgess, E., and Hanna, E.: Mass balance of the Greenland ice sheet from 1958 to 2007, Geophys. Res. Lett., 35, L20502, doi:10.1029/2008GL035417, 2008.

Rodell, M., Houser, P., Jambor, U., Gottschalck, J., Mitchell, K., Meng, C., Arsenault, K., Cosgrove, B., Radakovich, J., Bosilovich, M., Entin, J., Walker, J., Lohmann, D., and Toll, D.: The global land data assimilation system, B. Am. Meteorol. Soc., 85, 381–394, doi:10.1175/BAMS-85-3-381, 2004.

Schenk, T. and Csatho, B.: A new methodology for detecting ice sheet surface elevation changes from laser altimetry data, IEEE T. Geosci. Remote, 50, 3302–3316, 2012.

Schrama, E. and Wouters, B.: Revisiting Greenland ice sheet mass loss observed by GRACE, J. Geophys. Res., 116, B02407, doi:10.1029/2009JB006847, 2011.

Shepherd, A., Ivins, E., Geruo, A., Barletta, V., Bentley, M., Bettadpur, S., Briggs, K., Bromwich, D., Forsberg, R., Galin, N., Horwath, M., Jacobs, S., Joughin, I., King, M., Lenaerts, J., Li, J., Ligtenberg, S., Luckman, A., Luthcke, S., McMillan, M., Meister, R., Milne, G., Mouginot, J., Muir, A., Nicolas, J., Paden, J., Payne, A., Pritchard, H., Rignot, E., Rott, H., Sørensen, L., Scambos, T., Scheuchl, B., Schrama, E., Smith, B., Sundal, A., van Angelen, J., van de Berg, W., van den Broeke, M., Vaughan, D., Velicogna, I., Wahr, J., Whitehouse, P., Wingham, D., Yi, D., Young, D., and Zwally, H.: A reconciled estimate of ice-sheet mass balance, Science, 338, 1183–119, 2012.

Stober, M., Rawiel, P., Hepperle, J., and Wössner, R.: Long-term observations (1991–2011) of elevation change, and ice flow velocity in the Swiss-Camp area (West Greenland), IASC-NAG Workshop: The Dynamics, and Mass Budget of Arctic Glaciers, Geological Survey of Denmark, and Greenland Report, 3, 68–72, 2013.

Thomas, R., Csatho, B., Davis, C., Kim, C., Krabill, W., Manizade, S., McConnell, J., and Sonntag, J.: Mass balance of higher-elevation parts of the Greenland ice sheet, J. Geophys. Res., 106, 33707–33716, 2001.

van den Broeke, M., Bamber, J., Ettema, J., Rignot, E., Schrama, E., van de Berg, W., van Meijgaard, E., Velicogna, I., and Wouters, B.: Partitioning recent Greenland mass loss, Science, 326, 984–986, doi:10.1126/science.1178176, 2009.

Velicogna, I. and Wahr, J.: Greenland mass balance from GRACE, Geophys. Res. Lett., 32, L18505, doi:10.1029/2005GL023955, 2005.

Vernon, C. L., Bamber, J. L., Box, J. E., van den Broeke, M. R., Fettweis, X., Hanna, E., and Huybrechts, P.: Surface mass balance model intercomparison for the Greenland ice sheet, The Cryosphere, 7, 599–614, doi:10.5194/tc-7-599-2013, 2013.

Zwally, H., Li, J., Brenner, A., Beckley, M., Cornejo, H., DiMarzio, J., Giovinetto, M., Neumann, T., Robbins, J., Saba, J., Yi, D., and Wang, W.: Greenland ice sheet mass balance: distribution of increased mass loss with climate warming; 2003–07 vs. 1992–2002, J. Glaciol., 57, 88–102, 2011.

Zwally, H., Giovinetto, M., Beckley, M., and Saba, J.: Antarctic, and Greenland Drainage Systems, NASA GSFC Cryospheric Sciences Laboratory, available at: http://icesat4.gsfc.nasa.gov/cryo_data/ant_grn_drainage_systems.php (last access: December 2013), 2012.

Table 1. Mass balance by sector (Fig. 6) across Greenland and the Canadian Arctic, partitioned into ice sheet and peripheral glacier contributions. Uncertainty calculated as 1σ standard deviation across 1000 inversion simulations. Values have been rounded to the nearest Gt.

Sector	Ice Sheet (Gt a^{-1})	Peripheral Glaciers (Gt a^{-1})	Total (Gt a^{-1})
1	−24 ± 2	−7 ± 1	−30 ± 4
2	1 ± 2	0 ± 0	1 ± 2
3	−43 ± 5	−11 ± 2	−53 ± 7
4	−24 ± 2	−5 ± 2	−30 ± 2
5	−23 ± 2	−4 ± 1	−27 ± 2
6	−34 ± 2	−3 ± 0	−37 ± 3
7	−24 ± 1	−5 ± 1	−29 ± 2
8	−47 ± 4	−3 ± 0	−50 ± 4
9	0 ± 0	−29 ± 4	−29 ± 4
10	0 ± 0	−21 ± 4	−21 ± 4
Total	−217 ± 20	−88 ± 14	−316 ± 37

Table 2. Previously published in situ observations of mass balance ($\dot{m}$) throughout Greenland and the Canadian Arctic. Coffee can (C), strain network (S) and geodetic (G) techniques are denoted under method. * Denotes sites where the majority of the in situ observation period falls within the IMBIE period, permitting direct comparison to HIGA-inferred $\dot{m}$.

Site	°N	°E	$\dot{m}$ (m WE a^{-1})	Period	Method	Reference
Dye-3	65.18	−43.83	0.03 ± 0.06	c.1883–1983	S	1
South Dome	63.15	−44.82	0.122 ± 0.20	c.1950–2000	C	2
Saddle	66.00	−44.50	0.073 ± 0.18	c.1950–2000	C	2
Dye-2	66.50	−46.27	0.081 ± 0.16	c.1950–2000	C	2
Crawford Point	69.88	−46.97	−0.419 ± 0.23	c.1950–2000	C	2
Daugaard-Jensen	71.88	−32.05	−0.281 ± 0.20	c.1950–2000	C	2
Summit	72.57	−38.45	0.036 ± 0.02	c.1950–2000	C	2
NASA-U	73.83	−49.50	−0.022 ± 0.14	c.1950–2000	C	2
NASA-E	75.00	−30.00	0.061 ± 0.09	c.1950–2000	C	2
Camp Century	77.24	−61.03	−0.194 ± 0.17	c.1950–2000	C	2
Humboldt	78.53	−56.83	0.021 ± 0.06	c.1950–2000	C	2
Devon 1	75.34	−82.68	0.03 ± 0.04	c.1967–2007	S	3
Devon 2	75.18	−82.78	−0.05 ± 0.05	c.1967–2007	S	3
Devon 3	75.01	−82.88	−0.23 ± 0.07	c.1967–2007	S	3
Devon 1	75.34	−82.68	−0.02 ± 0.03	c.1967–2007	C	3
Devon 2	75.18	−82.78	−0.11 ± 0.05	c.1967–2007	C	3
Devon 3	75.01	−82.88	0.04 ± 0.06	c.1967–2007	C	3
Dye-3 Divide	64.85	−44.65	0.046 ± 0.075	1980–2011	G	4
Dye-3 East	65.26	−43.47	−0.055 ± 0.07	1980–2011	G	4
OSU West*	65.39	−47.67	−0.153 ± 0.075	2005–2011	G	4
OSU Central*	65.11	−45.69	−0.015 ± 0.075	2005–2011	G	4
Swiss Camp*	69.67	−49.43	−0.79 ± 0.04	2004–2011	G	5
ST2*	69.58	−49.78	−0.94 ± 0.05	2004–2011	G	5

[1] Reeh and Gundestrup (1985).
[2] Hamilton and Whillans (2002).
[3] Burgess and Sharp (2008).
[4] Jezek (2011).
[5] Stober et al. (2013).

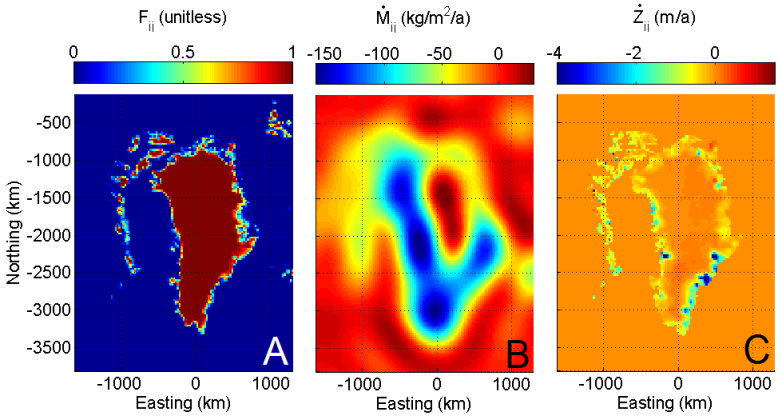

Fig. 1. Three independent pieces of information required as algorithm input. **(A)** Fractional ice coverage ($\dot{F}$), derived from glacier inventories generated by optical imagery (Arendt et al., 2012; Citterio and Ahlstrøm, 2013). **(B)** Spherical harmonic representation of cryosphere-attributed mass changes ($\dot{M}^{G}$), derived from gravimetry (Luthcke et al., 2013). **(C)** Ice surface elevation changes ($\dot{Z}$) derived from altimetry (Gardner et al., 2011; Schenk and Csatho, 2012). Map extent corresponds to inversion domain extent. Coordinates in polar stereographic projection.

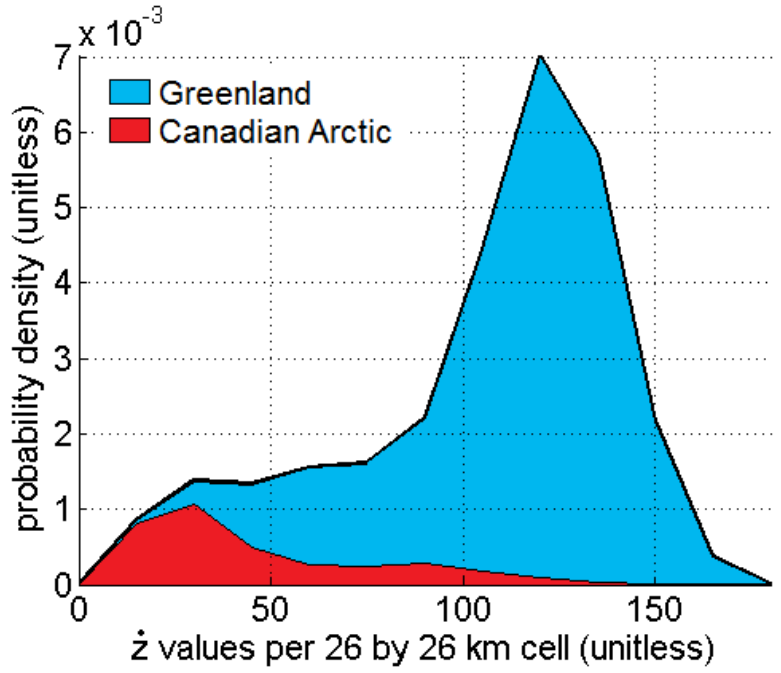

Fig. 2. Probability density functions of the altimetry-derived ice surface elevation change rates ($\dot{z}$, at 2 km resolution) observed per 26 by 26 km grid cell in both Greenland and the Canadian Arctic.

Discussion Paper | Discussion Paper | Discussion Paper | Discussion Paper |

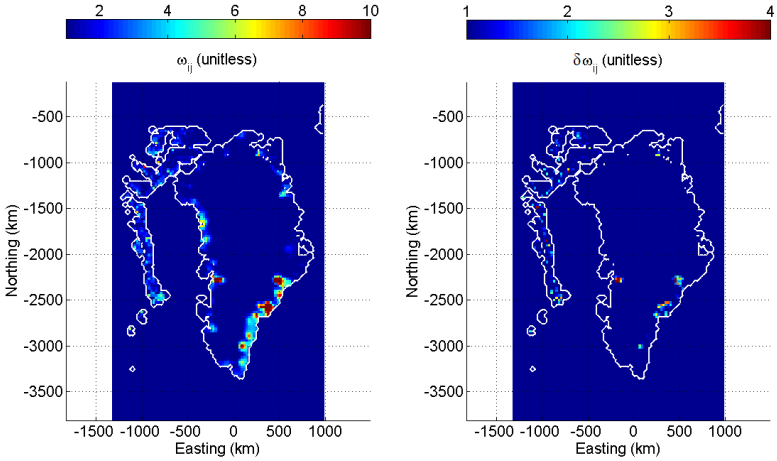

Fig. 3. Successive over relaxation (SOR)-type parameter (ω), and associated uncertainty ($\delta\omega$), derived from ice surface elevation changes observed by altimetry (Eqs. 3 and 4). White lines denote the perimeter of ice-containing nodes. Coordinates in polar stereographic projection.

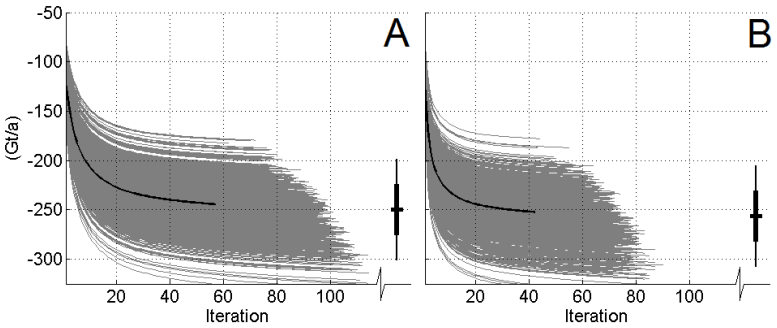

Fig. 4. Inversion simulations converging when rate of mass change over Greenland varies by less than 0.1 Gta^{-1} between iterations. Black line traces the ensemble mean until the first iteration when simulations begin to converge. The whisker plot at the right shows one and two standard deviations from the ensemble mean (thick and thin lines, respectively). **(A)** Under an $\omega = 1$ approach (Colgan et al., 2013). **(B)** Under implementation of a spatially variable SOR-type parameter (ω_{ij}; Fig. 3).

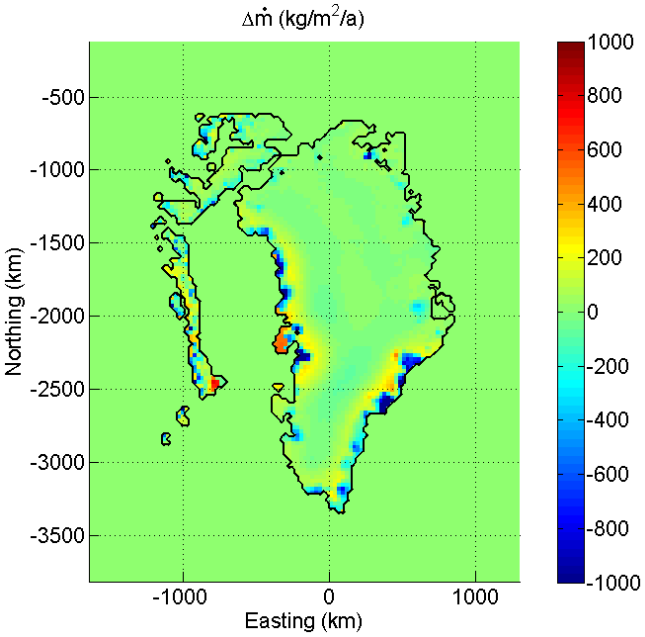

Fig. 5. Difference in specific mass balance ($\Delta\dot{m}$; e.g. *per unit ice area*) of the HIGA product, which includes altimetry-derived information, relative to the strict gravimetry-inversion product of Colgan et al. (2013), which does not include altimetry information. Black lines denote the extent of ice-containing nodes within the Canadian Arctic and Greenland. Coordinates in polar stereographic projection.

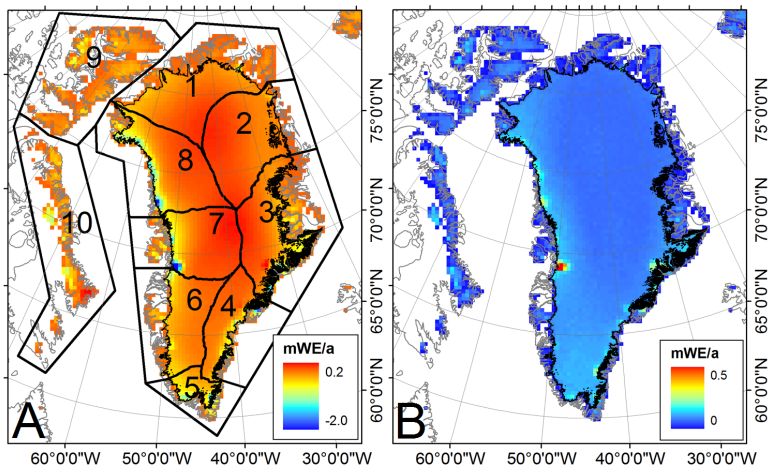

Fig. 6. (A) HIGA-inferred mass balance *per unit area* (i.e. rather than *per unit ice area*) across Greenland and the Canadian Arctic during the December 2003 to December 2010 period. **(B)** Associated uncertainty, defined as 1σ ensemble spread. Mass changes associated with ice sheet and peripheral glaciers and ice caps are assessed in ten geographic sectors (Table 1). Thin black line delineates the ice sheet margin.

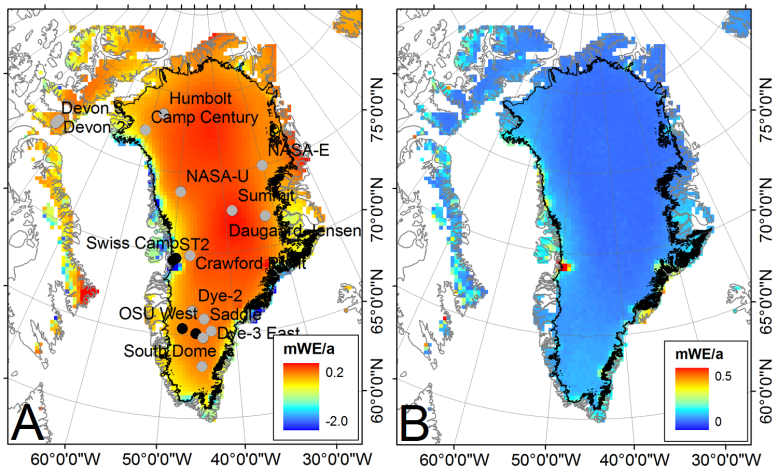

Fig. 7. (A) HIGA-inferred specific mass balance *per unit ice area* (i.e. rather than *per unit area*) across Greenland and the Canadian Arctic during the December 2003 to December 2010 (IMBIE) period. **(B)** Associated uncertainty, defined as 1σ ensemble spread. Inferred specific mass balance is compared with all available in situ observations of mass balance (Table 2). Black (grey) sites denote where the majority (minority) of the in situ observation period falls within the IMBIE period. Thin black line delineates the ice sheet margin.

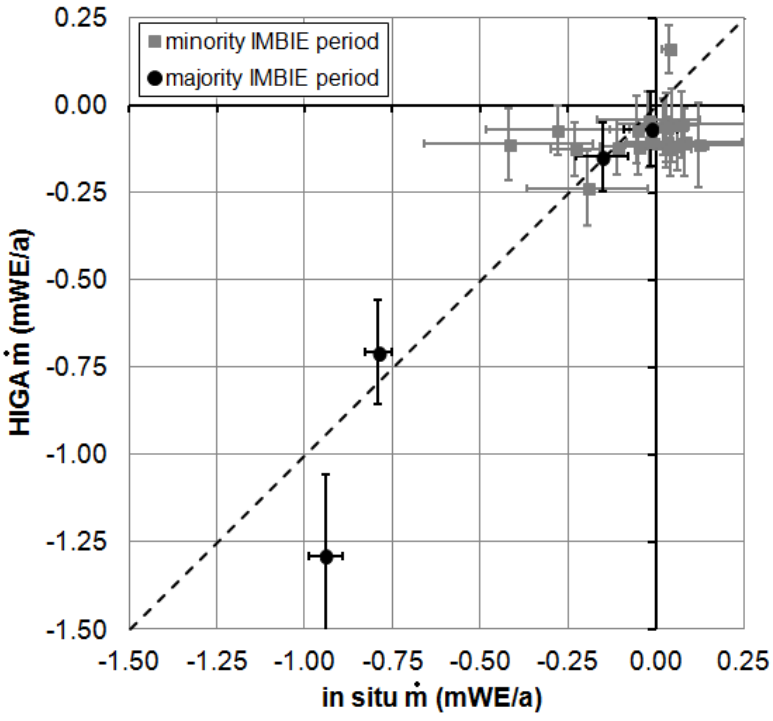

Fig. 8. Comparison of HIGA-inferred specific mass balance ($\dot{m}$) vs. in situ observations in Greenland and the Canadian Arctic (Table 2). Vertical and horizontal whiskers denote error in the HIGA product and in situ observations, respectively. Black (grey) sites denote where the majority (minority) of the in situ observation period falls within the December 2003 to December 2010 (IMBIE) period. Line $y = x$ shown for reference.

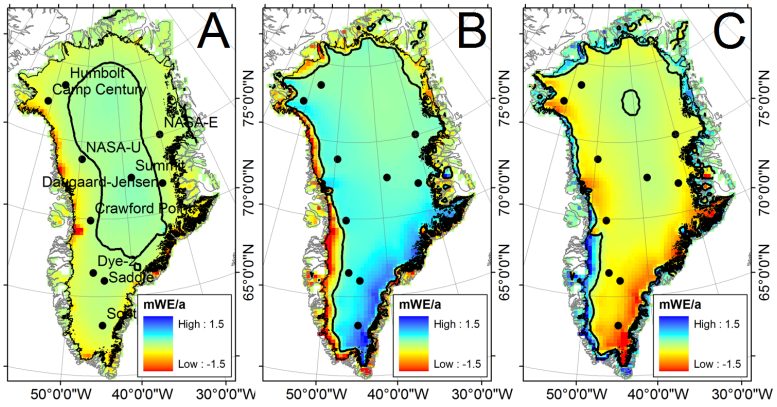

Fig. 9. IMBIE period (2004 to 2010) glacier continuity. **(A)** HIGA-inferred mass balance ($\dot{m}$; same as Fig. 6). **(B)** MAR modelled surface mass balance ($\dot{b}$). **(C)** Residual horizontal divergence of ice flux ($-\nabla Q$). The inverse ∇Q field is shown to maintain a convention of blue shading for mass gain and red shading for mass loss. Black dots denote in situ measurements of Hamilton and Whillans (2002). Black contours denote 0 m WE a^{-1}. All values given as *per unit area*.

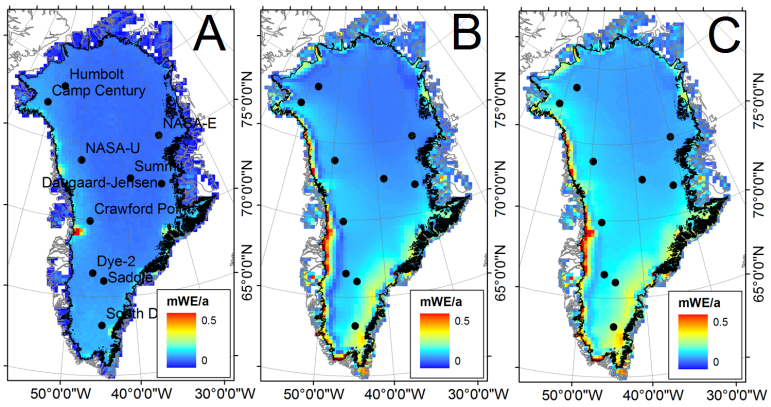

Fig. 10. (A) Uncertainty in HIGA-inferred mass balance ($\delta(\dot{m})$; same as Fig. 6). **(B)** Uncertainty in MAR modelled surface mass balance ($\delta(\dot{b})$; Fettweis et al., 2013). **(C)** Uncertainty in residual horizontal divergence of flux ($\delta(\nabla Q)$). Black dots denote in situ measurements of Hamilton and Whillans (2002). All values given as *per unit area*.

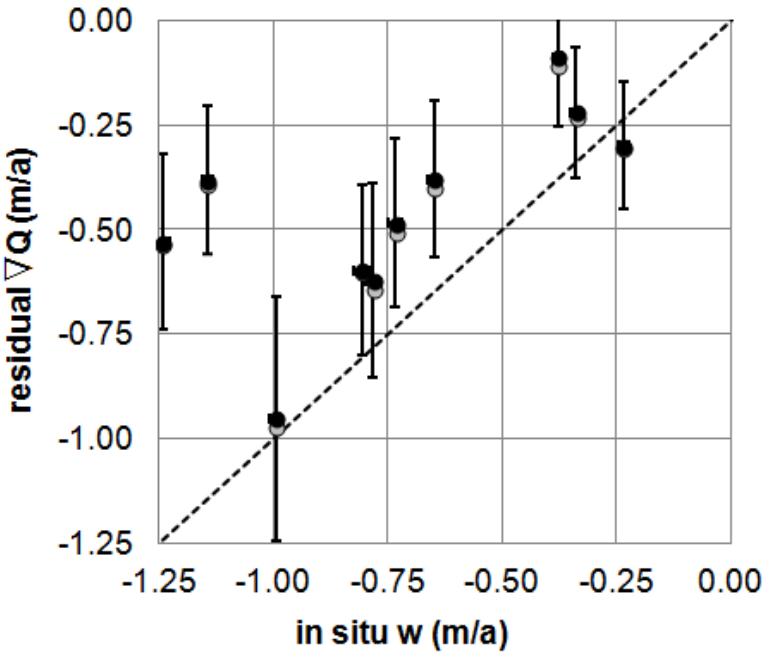

Fig. 11. Black dots denote residual divergence of ice flux ($-\nabla Q$; Eq. 7) vs. observed vertical ice velocity (w; Hamilton and Whillans, 2002). Grey dots reflect the incorporation of a 2 cm WE a^{-1} secular thickening trend above 2000 m. Vertical and horizontal whiskers denote associated uncertainty. Line $y = x$ shown for reference.

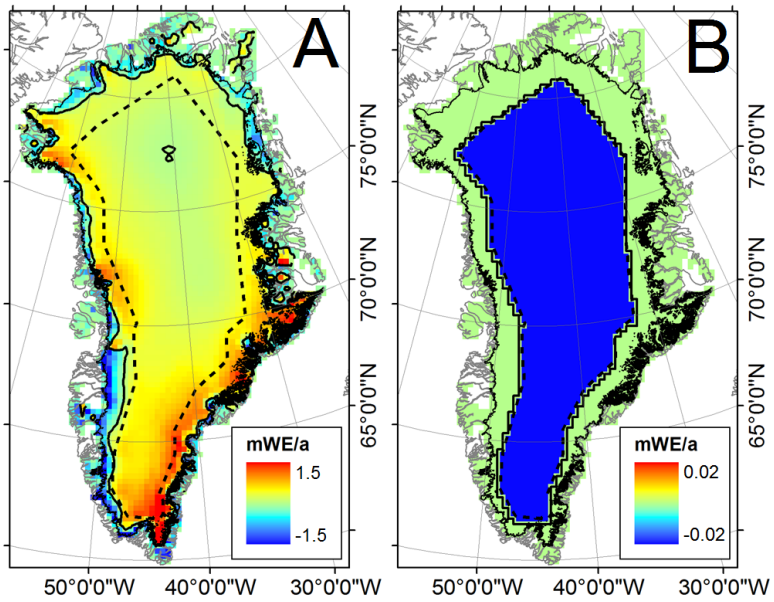

Fig. 12. Partitioning horizontal divergence of flux into shorter term (∇Q_{ST}; **A**) and longer term (∇Q_{LT}; **B**) ice dynamics according to Eq. (8). Solid line denotes 0 m WE a^{-1}. Dashed line denotes PARCA perimeter (Thomas et al., 2001). Inverse ∇Q fields are shown to maintain a convention of blue shading for mass gain and red shading for mass loss. Note different color scales.